Journal of Micro-Bio Robotics manuscript No.
(will be inserted by the editor)

Intuitive control of self-propelled microjets with haptic feedback

Claudio Pacchierotti · Veronika Magdanz · Mariana Medina-Sanchez · Oliver G. Schmidt · Domenico Prattichizzo · Sarthak Misra

Received: date / Accepted: date

Abstract Self-propelled microrobots have recently shown promising results in several scenarios at the microscale, such as targeted drug delivery and micromanipulation of cells. However, none of the steering systems available in the literature enable humans to intuitively and effectively control these microrobots in the remote environment, which is a desirable feature. In this paper we present an innovative teleoperation system with force reflection that enables a human operator to intuitively control the positioning of a self-propelled microjet. A particle-filter-based visual tracking algorithm tracks at runtime the position of the microjet in the remote environment. A 6-degrees-of-freedom haptic interface then provides the human operator with compelling haptic feedback about the interaction between the controlled microjet and the environment, as well as enabling the operator to intuitively control the target position of the microjet. Finally, a wireless magnetic control system regulates the orientation of the microjet to reach the target point. The viability of the proposed approach is demonstrated through two experiments enrolling twenty-eight subjects. In both experiments providing haptic feedback significantly improved the performance and the perceived realism of the considered tasks.

Keywords microtechnology · haptics · teleoperation · actuators · robotics

This project (ROBOTAR) has received funding from the European Research Council (ERC) under the European Union's Horizon 2020 Research and Innovation programme (Grant Agreement #638428). The research leading to these results has also received funding from the European Union Seventh Framework Programme FP7/2007-2013 under grant agreement #601165 of project "WEARHAP - WEARable HAPtics for humans and robots".

C. Pacchierotti (✉)
Dept. of Advanced Robotics, Istituto Italiano di Tecnologia, Genova, Italy.
E-mail: pacchierotti@diism.unisi.it

V. Magdanz
Institute for Integrative Nanosciences, IFW Dresden, Dresden, Germany.
E-mail: v.magdanz@ifw-dresden.de

M. Medina-Sanchez
Institute for Integrative Nanosciences, IFW Dresden, Dresden, Germany.
E-mail: m.medina.sanchez@ifw-dresden.de

O. G. Schmidt
Institute for Integrative Nanosciences, IFW Dresden, Dresden, Germany
Material Systems for Nanoelectronics, University of Technology Chemnitz, Chemnitz, Germany.
E-mail: o.schmidt@ifw-dresden.de

D. Prattichizzo
Dept. of Information Engineering and Mathematics, University of Siena, Siena, Italy
Dept. of Advanced Robotics, Istituto Italiano di Tecnologia, Genova, Italy.
E-mail: prattichizzo@diism.unisi.it

S. Misra
Surgical Robotics Laboratory, Department of Biomechanical Engineering, MIRA - Institute for Biomedical Technology and Technical Medicine, University of Twente, Enschede, The Netherlands.
Department of Biomedical Engineering, University of Groningen and University Medical Centre Groningen, Groningen, The Netherlands.
E-mail: s.misra@utwente.nl

1 Introduction

The development of artificial micromotors has been progressing fast since the last decade and promising results have been achieved regarding several robotic tasks at the microscale, such as controlled micropositioning [1,2,3], pickup and delivery of micro-objects, cells, and molecules [4,5,6,7,8], and drilling into soft tissue [9,10,11,12]. Moreover, artificial micromotors have been proved to be of potential interest for applications in environmental science [9,13], sensing [7,8,14,15], and drug delivery [16,17]. Several types of catalytic microrobots have been demonstrated to overcome Brownian

motion at low Reynolds number regimes [1, 18, 19]. Motion of these microrobots is based on several propulsion mechanisms, originated mainly from self-electrophoresis [20], self-diffusiophoresis [21], interfacial tension [22], and microbubbles. Microjets are tubular micromotors of this last type that are able to move at high speeds in hydrogen peroxide solutions (up to 200 body lengths per second [23]). They are fabricated from rolled up nanomembranes of titanium, chromium, iron, and platinum. Their propulsion is based on the catalytic decomposition of hydrogen peroxide by thin layers of platinum, which generates bubbles and leads to the fast forward jet motion of the microtube (see Sec. 3.1.1 for details on the fabrication and propulsion mechanism of the microjets).

One of the challenges in the development of micromachines for manipulation tasks at the microscale is the precise and quick remote control of these micromotors. In this respect, Khalil et al. [24] presented a system for the 2-dimensional (2-D) closed-loop motion control of self-propelled microjets using four iron-cored electromagnetic coils and feedback extracted from a microscopic vision system. The system controlled the orientation of the microjets using external magnetic torque, whereas the linear motion toward a reference position was accomplished by the thrust and pulling magnetic forces generated by the ejecting oxygen bubbles and field gradients, respectively. The control system navigated the microjets at an average velocity of 115 μm/s and within an average region-of-convergence (ROC) of 365 μm. Sanchez et al. [25] presented a 2-D closed-loop control of self-propelled microjets using feedback extracted from B-mode ultrasound images. In this case, only two iron-cored electromagnetic coils were used to generate the steering torques within a plane. Coil currents were calculated using the position error between the target position and the position registered by the ultrasound machine. The control system positioned microjets at an average velocity of 156 μm/s with an average tracking error of 250.7 μm. Khalil et al. [26] presented a system for the closed-loop motion control of self-propelled microjets inside a fluidic microchannel. In the absence of a fluid flow, the control system positioned the microjets at an average velocity of 119 μm/s and within an average ROC of 390 μm. With a flow rate of 2.5 μl/min applied against the direction of the microjets, the control system positioned the microjets at an average velocity of 90 μm/s and within an average ROC of 600 μm.

However, although quite effective, none of these systems enable humans to intuitively and effectively steer the microjets in remote environments. The above mentioned works, in fact, only take into account autonomous approaches. Nonetheless, for reasons of safety, responsibility, and public acceptance, it would be beneficial to provide a human operator with intuitive means for directly controlling the motion of a microjet, especially when dealing with medical

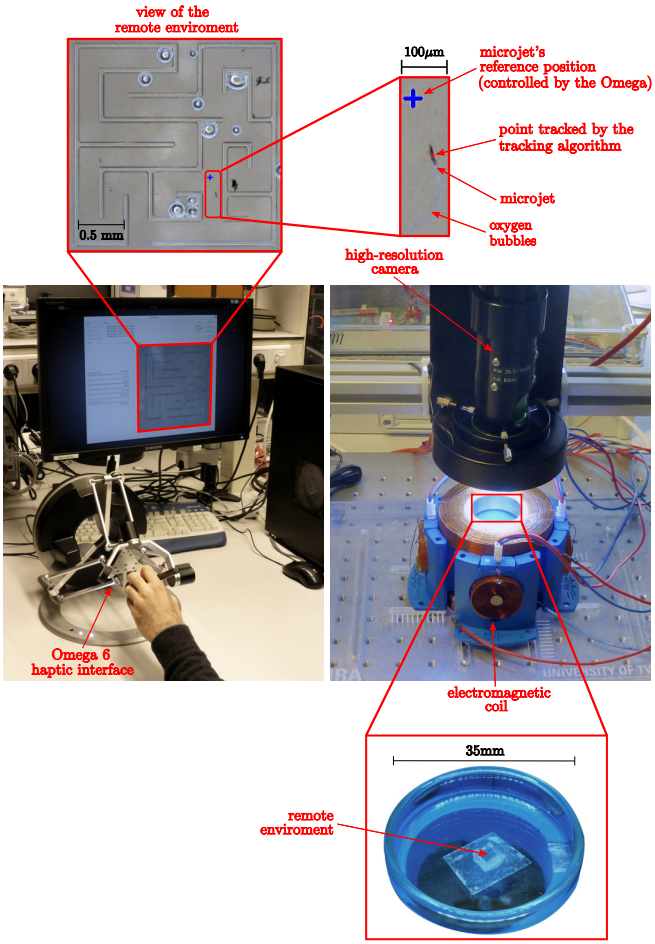

Fig. 1 Experimental setup: The tracker measures at runtime the position of the microjets in the remote environment. The human operator then sets the microjet's reference point by controlling the position of the end-effector of a 6 DoF haptic interface. At the same time, according to the feedback condition being considered, the human operator is also provided with kinesthetic and/or vibrotactile force feedback through the end-effector of the same haptic interface. Finally, the magnetic control system regulates the orientation of the microjet toward the reference point.

applications [27, 28, 29]. In such a case, the operator needs to observe, from the master side, the environment within the controlled microjet is moving. This is possible through different types of information that flow from the remote scenario to the human operator. They are usually a combination of visual and haptic stimuli. Visual feedback is already employed in several commercial telerobotic systems (e.g., the da Vinci Surgical System, Intuitive Surgical, USA) while it is not common to find commercially-available teleoperation systems implementing haptic force feedback. This omission is mainly due to the fact that in certain situations haptic feedback can lead to an unstable behavior of the system. Indeed, stability of teleoperation systems with force reflection can be significantly affected by communication latency in the loop, hard contacts, relaxed grasps, and many other destabilizing

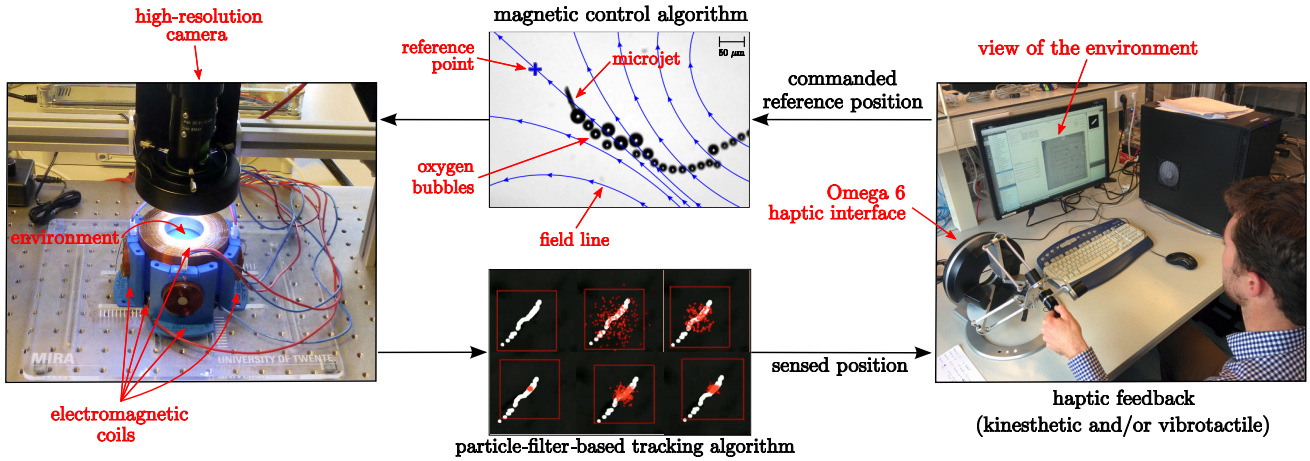

Fig. 2 Teleoperation system: The image-guided tracking algorithm tracks at runtime the position of the microjets in the remote environment using a high-resolution camera and a particle-filter-based algorithm. A 6-DoF grounded haptic interface then provides the human operator with haptic feedback, kinesthetic and/or vibrotactile, about the interaction of the microjet with the remote environment. At the same time, it enables the operator to intuitively control the reference position of the microjet. Finally, the magnetic control algorithm controls the orientation of the microjet, steering it toward the reference position defined by the operator.

factors that dramatically reduce the effectiveness of haptics in teleoperation [30].

Nonetheless, haptic feedback is still widely believed to be a valuable tool in teleoperation [31,32,33,34,35]. Its benefits typically include increased manipulation accuracy [36, 37], and decreased completion time, peak and mean force applied to the remote environment [36,38,39,40,41]. In medical scenarios, force feedback has been proved to improve performance in fine microneedle positioning [42], telerobotic catheter insertion [43], suturing simulation [44], cardiothoracic procedures [45], and cell injection systems [46]. The benefits of haptic feedback have been also shown in micromanipulation [47,48,49,50]. Mehrtash et al. [48], for example, presented a magnetic micromanipulation platform able to provide haptic feedback through a Phantom Omni haptic interface (Geomagic, USA). The human operator feels a resistive force every time the microrobot encounters a stiff object. More recently, Ghanbari et al. [50] developed a microrobotic teleoperated cell injection system that provides the human operator with position-to-position kinematic mapping between master and slave, as well as haptic guidance for real-time assistance during the injection task.

To guarantee the stability of teleoperation systems with force reflection, passivity [51] has been exploited as the main tool for providing a sufficient condition for stable teleoperation in several controller design approaches [52,53,54, 55]. In [52], for example, a coding scheme is applied to the power variables (velocities and forces) to turn the time-delayed communication channel into a passive element. More recently, Franken et al. [55] presented a dual-layer controller structure. A transparency layer is in charge of computing the ideal forces to be actuated at both the master and the slave, regardless of stability constraints. Cascaded with the transparency layer, a passivity layer modulates such forces when this is necessary to avoid violations of the passivity condition. A further approach to provide force information in teleoperation while guaranteeing the stability of the control loop is *sensory substitution*. It consists of substituting haptic force with alternative forms of feedback, such as vibrotactile [56], auditory [41], and/or visual feedback [57]. In this case, since no haptic force is fed back to the operator, the control loop is stable and no bilateral controller is thus needed [37]. Kitagawa et al. [57], for example, discussed the effects of substituting haptic feedback with visual and auditory cues during a teleoperated surgical knot-tying task. Forces applied while using these sensory substitution modalities more closely approximate suture tensions achieved under ideal haptic conditions (i.e., hand ties) than forces applied without such feedback. Ramos et al. [58] combined haptic feedback and sensory substitution via vibrotactile stimuli in a teleoperated needle insertion task to convey multiple pieces of information through the same perception channel, i.e., the skin. They provided the human operator with vibrotactile feedback to render navigation cues and haptic feedback to reproduce the mechanical properties of the tissue being penetrated. Similarly, Pacchierotti et al. [28] presented a teleoperation system for steering flexible needles that enables clinicians to directly maneuver the surgical tool while providing them with navigation cues through haptic and vibrotactile force feedback.

1.1 Contribution

In this study we present an innovative haptic teleoperation system for steering self-propelled microjets in 2-dimensional space, shown in Fig. 1. It enables a human operator to in-

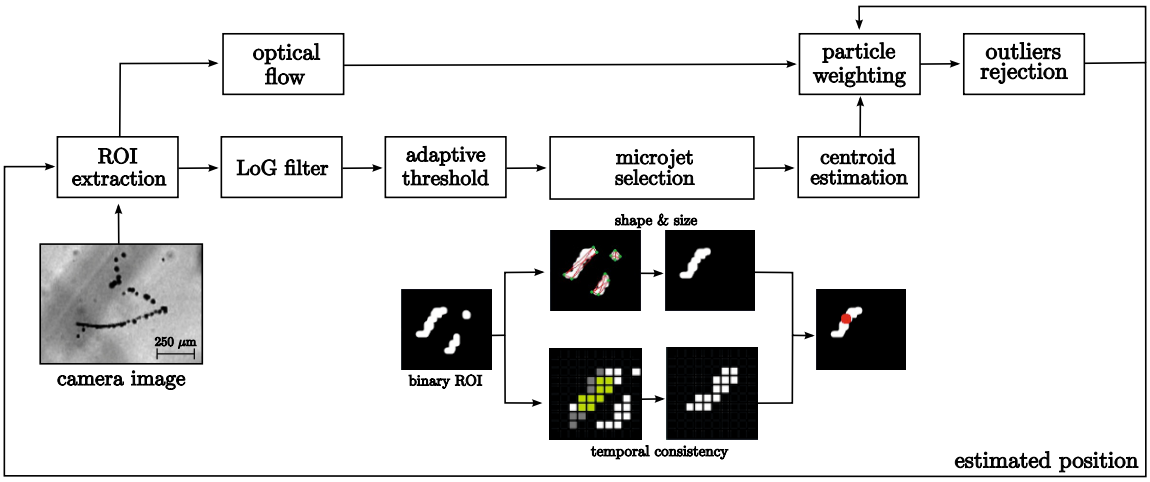

Fig. 3 Tracking algorithm. Each region of interest (ROI) registered by the camera is first filtered by a Laplacian of Gaussian (LoG) filter. Subsequently, the tracker selects the target object based on shape, size, and temporal consistency, and it then estimates its position. Finally, to robustly track inconsistent shapes and to effectively reject the presence of other microjets that we do not want to control, we use a particle filter. The tracker uses the estimated position to weight the particles of the particle filter. After the weighting, the particles are also used for position estimation in the next frame.

tuitively and accurately control the motion of a microjet in the remote environment while providing him/her with compelling haptic feedback about the interaction between the microjet and said environment.

An image-guided tracking algorithm tracks at runtime the position of the microjets using a high-resolution camera and a particle-filter-based algorithm, as described in Sec. 2.1. A 6 degrees-of-freedom (DoF) grounded haptic interface then provides the human operator with haptic feedback about the interaction between the controlled microjet and the remote environment, as well as enabling him/her to intuitively control the reference target position of the microjet, as described in Sec. 2.2. Finally, the control algorithm controls the orientation of the selected microjet using magnetic torques generated by six electromagnetic coils, which steer the microjet toward the reference position defined by the operator, as summarized in Sec. 2.3. Figure 2 shows how the tracking, haptic, and control systems are interconnected. While the magnetic control system has been adapted from [24], tracking and haptic rendering systems are presented here for the first time.

Together with the teleoperation system, we also present two innovative force rendering algorithms able to provide information about the interaction between the microjet and the remote environment in the case of both structured and unstructured environments. We employ an adapted version of the god-object model [59] in the case of structured remote environments, while we estimate the interaction forces from the change in velocity of the microjet in the case of unstructured environments. Finally, we also present the evaluation of three different types of tactile and kinesthetic haptic force feedback, with the objective of discovering the most effective rendering approach for the considered application. To the best of our knowledge, this is the first time that the effectiveness of haptics is tested in such an application.

2 Teleoperation System

The teleoperation system is composed of the tracking, haptic, and control systems summarized below. They enable a human operator to intuitively and accurately control the motion of a microjet in 2-dimensional space while providing him or her with compelling haptic feedback about the interaction of the microjet with the remote environment.

2.1 Tracking System

In order to precisely track the position of the controlled microjet in the remote environment, we placed a high-resolution camera above the Petri dish hosting the environment (see Fig. 1). The camera is a Sony XCD-X710 1024×768 pixels FireWire videocamera (Sony Corporation, Japan). It has an adjustable zoom with a maximum of 24X, a frame rate of 25 fps, and it is mounted on a linear stage to enable precise focusing. A CCD sensor is used for recording, with a pixel width and height of 5.50 μm, providing a resolution up to 0.50 μm. The flow chart of the tracking algorithm is shown in Fig. 3.

2.1.1 Object recognition

Each frame registered by the camera is first filtered by a Laplacian of Gaussian (LoG) filter [60], which is used to find areas of rapid change (edges) in the image. The purpose of this preprocessing technique is to make the algorithm less

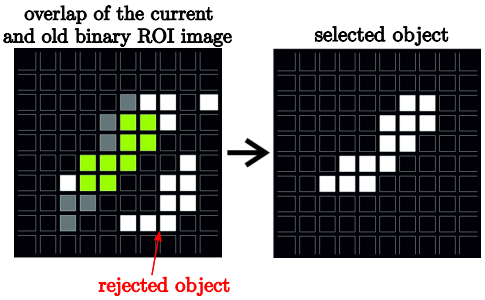

Fig. 4 Time consistency within a region of interest (ROI). In the left picture an overlap of the current and old binary ROI images is shown. White pixels from the old binary image of the ROI are shown in gray, white pixels from the current ROI are shown in white, and overlapping pixels are shown in green. Two objects are present in the current ROI (left), but, since the object in the middle has the most overlapping pixels, the tracker rejects the other one (right).

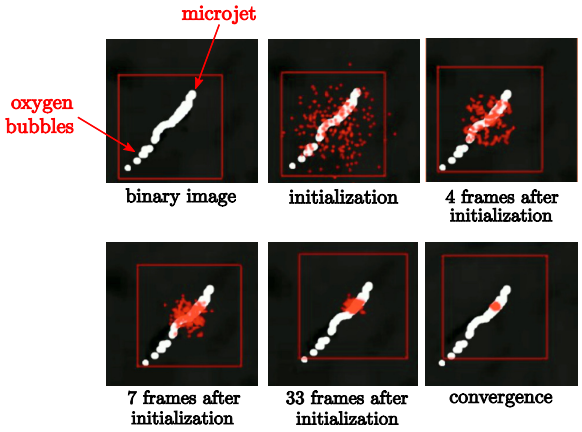

Fig. 5 Convergence of the particle filter on a microjet. The particle filter provides robust tracking even in the presence of inconsistent shapes such as a microjet surronded by its own oxygen bubble trail. The tracker achieves a frame rate of approximately 30 frames per second.

sensitive to artifacts and noise, including shadows, reflections and features outside the focus of the camera, with the objective of making the algorithm more sensitive to the features of the target microrobot. A custom LoG filter can be designed for each type of microrobot by choosing an appropriate standard deviation σ for the LoG filter kernel, evaluated as

$$\mathrm{LoG}(x,y) = \frac{1}{\pi\sigma^4}\left(1-\frac{x^2+y^2}{2\sigma^2}\right)e^{-\frac{x^2+y^2}{2\sigma^2}}, \quad (1)$$

where $\mathrm{LoG}(0,0)$ is the midpoint of the kernel, and x and y are the pixel coordinates of the 2-D frame recorded by the CCD sensor. The filtered frame $F_f(x,y)$ is then converted to a binary frame $F_b(x,y)$ using a simple adaptive threshold,

$$F_b(x,y) = \begin{cases} 1 & \text{if } F_f(x,y) < T(x,y) \\ 0 & \text{otherwise,} \end{cases} \quad (2)$$

where $T(x,y)$ is the threshold matrix, that is properly tuned for each type of microrobot. Pixels equal to zero are colored as white, while pixels equal to one are colored as black (see Figs. 4 and 5). Once the binary frame is obtained, objects that are most likely to be microrobots are selected according to their size and shape. Finally, the estimated position of their centroids is calculated by averaging their pixel coordinates. In this work we customized the filter and the threshold matrix for the tracking of self-propelled microjets.

2.1.2 *Region of interest*

In order to reduce the overall computational complexity, once we have selected the microrobots to track, instead of analyzing the full-size frame, we can choose a region of interest (ROI) around each tracked object, in which the tracking analysis is carried out. The size of the ROI is fixed and determined a priori according to the size and speed of a microjet, so that it contains the tracked object for at least two consequent frames. The center of the ROI is the estimated position of the considered microrobot's centroid, and it is updated at every cycle. If multiple objects appear within a ROI, the tracker select the object that is temporally the most consistent. This is done by segmenting the binary image of the ROI and comparing the overlapping pixels between the current image and the previous one, as illustrated in Fig. 4.

2.1.3 *Particle filter*

Although the object recognition technique described above can already provide a good position estimation in case of high contrast frames (e.g., magnetic microparticles under a microscope), in our application we require the tracker to robustly track inconsistent shapes, such as our microjets surrounded by oxygen bubble trails. The inability to do so may in fact lead to a wrong mapping of the magnetic forces, which would affect the positioning of the microjet (see Sec. 2.3), and to abrupt changes in the position of the haptic device end-effector, which would dramatically reduce the quality of the haptic interaction (see Sec. 3). For this reason, in order to robustly track self-propelled microjets, we employed a particle filter [61], which is a sequential version of the Monte Carlo algorithm. At the beginning, the particles of the particle filter are seeded with a Gaussian distribution around the selected microjet, based on the a priori knowledge of the microjet speed [23]. Independent distributions are used on both directions, since the direction of the movement is not known yet. The distributions are generated by taking the Box-Muller transform of uniformly distributed random numbers $\mathbf{u_1}$ and $\mathbf{u_2}$, adjusting the mean and standard deviation of the distributions according to the position of the centroid and the speed of the microjet, respectively. Given a particle set $\mathbf{N} = [\mathbf{N_{pos}} \quad \mathbf{N_{weight}}]^{\mathrm{T}}$, we can thus define the initial particles

positions as

$$\mathbf{N_{pos}} = \begin{bmatrix} x_c + \sqrt{-2\ln(\mathbf{u_1})}\cos(2\pi\mathbf{u_2})\sigma_s \\ y_c + \sqrt{-2\ln(\mathbf{u_1})}\sin(2\pi\mathbf{u_2})\sigma_s \end{bmatrix}^{\mathrm{T}} = \begin{bmatrix} \mathbf{N_{pos,x}} \\ \mathbf{N_{pos,y}} \end{bmatrix}^{\mathrm{T}}, \quad (3)$$

and their initial weights as $\mathbf{N_{weight}} = \mathbf{1}$. Coordinates (x_c, y_c) indicate the position of the microjet's centroid, as estimated in Sec. 2.1.1, and σ_s indicates the expected standard deviation of the microjet speed.

After this initialization, at each new cycle, the weight of each particle i is calculated using the estimated position of the tracked object based both on the abovementioned centroid estimation and on the optical flow, i.e.,

$$N_{\text{weight}}(i) = p_c(i)p_o(i), \quad (4)$$

where

$$\begin{aligned} p_c(i) &= \frac{1}{\sigma_c\sqrt{2\pi}} e^{-\frac{1}{2}\left(\left(\frac{N_{pos,x}(i)-x_c}{\sigma_c}\right)^2+\left(\frac{N_{pos,y}(i)-y_c}{\sigma_c}\right)^2\right)} \\ p_o(i) &= \frac{1}{\sigma_o\sqrt{2\pi}} e^{-\frac{1}{2}\left(\left(\frac{N_{pos,x}(i)-x_o}{\sigma_o}\right)^2+\left(\frac{N_{pos,y}(i)-y_o}{\sigma_o}\right)^2\right)}. \end{aligned} \quad (5)$$

Coordinates (x_c, y_c) and (x_o, y_o) indicate the estimated position of the target microjet according to the object recognition method of Sec. 2.1.1 and the optical flow, respectively. σ_c and σ_o represent the standard deviations of these estimations, respectively. The optical flow estimation, which assumes that neighboring pixels have similar motion, is done according to the Lucas-Kanade method [62]. After the weighting, each particle is split into particles of equal weight, and, since the number of particles is not changing, particles with low weights are excluded and particles with high weights result in a stack of multiple particles. An example of the convergence of the particle filter on a microjet is shown in Fig. 5.

Although this tracking algorithm supports many different types of microrobots, such as Janus particles and microparticles, in this work we have tuned it for the tracking of self-propelled microjets. Experiments showed the tracker to be able to track microjets in 2-D with an average precision of 90.4 μm at 25 Hz [**?**].

During the experiments described in this paper, the microjet to control was manually selected at the beginning of each set of experiments with one subject, and the tracking was never lost throughout the trails.

2.2 Haptic System

The haptic feedback system is a 6-DoF Omega haptic interface (Force Dimension, Switzerland), shown in Fig. 6. It is composed of a delta-based parallel kinematics structure that provides good closed loop stiffness and high accuracy. The rotating wrist joint allows the user to also change the orientation of the pen-shaped end-effector. Moreover, the interface is constructed in such a way that translations and rotations are decoupled from each other. Translational degrees of freedom are active, while rotational degrees of freedom are passive. This haptic interface is also equipped with active gravity compensation to improve the teleoperation transparency and reduce the operator's fatigue. In this work we use the Omega 6 interface as an impedance haptic device. We measure the position of the end-effector, controlled by the human operator, to set the reference target position of the microjet. The scaling factor between master and slave systems is 0.03 in all directions, i.e., moving the end-effector of the Omega interface of 10 cm moves the microjet's reference position of 3 mm. At the same time, through the same end-effector, we provide the operator with force feedback from the remote environment. The force to be provided is evaluated according to the feedback condition considered, as detailed in Sec. 3, and it is a combination of kinesthetic and vibrotactile stimuli. The haptic control loop runs at 2 kHz.

Since we control the microjet in 2-dimensional space, the translational motion of the Omega is constrained on a x-y plane (see Fig. 6). Force $f_z(t)$, provided by the Omega interface along the z axis, is defined as

$$f_z(t) = -k_{b,k}(p_{o,z}(t) - p_{z,plane}),$$

where $k_{b,k} = 2000$ N/m, $p_{o,z}(t)$ is the current position of the end-effector of the Omega in the z direction, and $p_{z,plane}$ is the location of the x-y plane along z. The Omega's pen-shaped end-effector is also equipped with a programmable button. For safety reasons, the position of the Omega's end-effector is linked with the reference target position of the microjet *only* when the button is pressed. On the other hand, when the button is not pressed, the translational motion of the Omega is blocked and the movements of the end-effector are not forwarded to the control system. Force $\mathbf{f_b}(\mathbf{t}) \in \mathbb{R}^2$, provided by the Omega interface along the x and y directions when the button is not pressed, is defined as

$$\mathbf{f_b}(\mathbf{t}) = -k_{b,k}(\mathbf{p_o}(\mathbf{t}) - \mathbf{p_{o,b}}),$$

where $\mathbf{p_o}(\mathbf{t}) \in \mathbb{R}^2$ is the current position of the end-effector of the Omega, and $\mathbf{p_{o,b}} \in \mathbb{R}^2$ is the position of the end-effector of the Omega the instant the button was released.

Although a 6-DoF haptic interface may seem unnecessary to control microjets in 2-D, pilot experiments showed the three rotational degrees of freedom to improve the operator's comfort and ergonomy with respect to interfaces with fewer degrees of freedom, e.g., the 3-DoF Omega 3 interface by Force Dimension.

2.3 Control System

Given the current position of the microjet, as estimated by the tracking algorithm, and the commanded reference position,

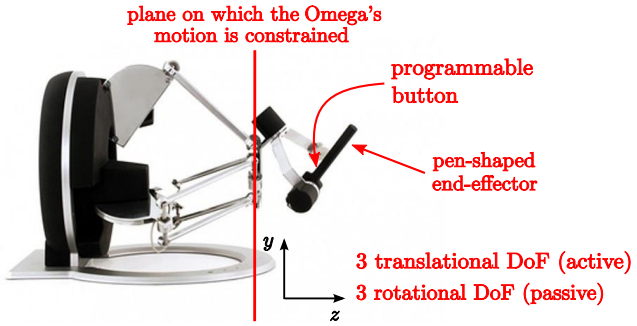

Fig. 6 The Omega 6 haptic interface provides the human operator with haptic feedback from the remote environment and, at the same time, provides the control system with the microjet's reference position. The haptic feedback provided is a combination of kinesthetic and vibrotactile stimuli, depending on the feedback modality considered (see Sec. 3). Since the microjets are controlled in 2-dimensional space, we constrained the translational motion of the Omega to its *x*-*y* plane.

as controlled by the operator through the end-effector of the haptic interface, the control system controls the orientation of the microjet through an array of six orthogonally oriented metal-core electromagnets, with the aim of steering it toward the reference point.

The electromagnetic system controls the orientation of the selected microjet using external magnetic torque, whereas the forward motion towards the reference position is accomplished by the thrust force generated by the ejecting oxygen bubbles. In particular, we employ a sliding-mode control system [63], owing to its robustness in the presence of parameter uncertainties and unmodeled disturbance forces, such as wall and surface effects, bubbles-microjet interactions, and microjet-microjet interactions. At first, we characterize the magnetic dipole moment based on the motion analysis of the microjets using uniform magnetic field reversals [64]. Then, we employed the characterized magnetic dipole moment for the realization of a magnetic force-current map of the microjet. This map, in turn, is used for the design of a closed-loop control system that does not depend on the exact dynamical model of the microjets and the accurate knowledge of the parameters of the magnetic system. The motion control characteristics in the transient- and steady-states depend on the concentration of the surrounding fluid (hydrogen peroxide solution) and the strength of the applied magnetic field. The control system has been presented in [2,26,24], and it has been proved to position microjets at an average velocity of 115 μm/s, and within an average region-of-convergence of 365 μm. The control algorithm loop runs at 100 Hz. A video of a microjet being controlled in free space is available as supplemental material.

The teleoperation system is managed by a GNU/Linux machine (Debian 7.4 with Linux Kernel 3.2), equipped with a real-time scheduler. The haptic device and the high-resolution camera are connected to the GNU/Linux machine via USB and Ethernet connections, respectively. The electromagnets are driven by a custom control board that provides the required current. The image-guided tracking algorithm tracks at runtime the position of the microjets in the remote environment at 25 Hz. The 6-DoF grounded haptic interface then provides the human operator with haptic feedback about the interaction of the microjet with the remote environment at 2 kHz. Finally, the magnetic control algorithm controls the orientation of the microjet at 100 Hz, steering it toward the reference position defined by the operator. The haptic interface therefore receives for 80 cycles the same information from the tracker and, although the reference position of the microjet is updated at 2 kHz, the magnetic controller changes it every 0.01 s only. Similarly, the control algorithm receives for 4 cycles the same information from the tracker.

So as to preserve the stability of the teleoperation system, we took into account the passivity controller described in [55] (see also Sec. 1). The control architecture is split into two separate layers. The hierarchical top layer, named *Transparency Layer*, aims at achieving the desired transparency, while the lower layer, named *Passivity Layer*, ensures the passivity of the system. Separate communication channels connect the layers at the slave and master levels so that information related to exchanged energy is separated from information about the desired behavior. The parameters used in our implementation of this control strategy are the same employed in [28]. Stability control is only used to regulate the *kinesthetic* force feedback provided by the haptic interface (see Sec. 3), since vibrotactile stimuli do not affect the stability of the control loop [37].

3 Experimental Evaluation

This section presents the experimental evaluation of the integrated teleoperation system with haptic feedback. The experimental setup is shown in Figs. 1 and 2. It is composed of the tracking, haptic, and control systems detailed in Sec. 2. In order to test the effectiveness of our system and to understand the role of haptic feedback for such an application, we carried out two sets of experiments. The first one, described in Sec. 3.2, aims at evaluating the steering capabilities of the proposed teleoperation system in a structured remote environment composed of a 2.25×2.25 mm maze. The second experiment, described in Sec. 3.3, aims at evaluating the steering capabilities of our system in an unstructured remote environment composed of randomly placed microstructures. In both experiments the environment is filled with hydrogen peroxide solution with concentration of 5%, along with small amounts of isopropanol and Triton X. A catalytic microjet with a length of 50 μm is used.

3.1 Materials

3.1.1 Microjets fabrication and propulsion mechanism

Catalytic microjets are fabricated from rolled up nanomembranes of titanium, chromium, iron and platinum. At first, 18×18 mm glass wafers are cleaned with acetone and isopropanol by sonication for 2 minutes in each solvent. The glass wafers are dried and baked at 120°C for 2 minutes. Coating with positive photoresist ARP-3510 is carried out on a spin-coater at 3500 rpm for 35 seconds. The samples are post baked at 90°C for 2 minutes. Exposure to ultraviolet light through a mask of 50×50 μm squared structures for 7 seconds with a MJB 4 Mask Aligner leads to photolithographic patterning of the photoresist. The samples are developed in AR 300-35: water (1:1) solution for 50 seconds and dried subsequently. Angled metal evaporation of 5 nm titanium, 5 nm chromium and 5 nm iron at different rates (3Å/s, 0.5 Å/s, 1 Å/s) is conducted on each of these patterned wafers using an Edwards E-beam. Subsequent sputtering of 3 nm of platinum is performed by using magnetron sputtering machine. The sacrificial photoresist layer is removed by immersing the glass wafers in isopropanol. The Ti/Cr/Fe/Pt nanomembranes roll up immediately into microtubes of 50 μm length.

The motion of these microjets is based on the catalysis of hydrogen peroxide on the inner platinum tube wall, which generates bubbles and leads to the fast forward jet motion of the microtube. If a catalyst is present, in fact, hydrogen peroxide is rapidly converted into oxygen and water. The formation of oxygen bubbles inside the tube cavity leads to the accumulation and, finally, to the ejection of bubbles from one end of the microtube. This ejection of bubble creates a forward motion of the microtube in the opposite direction of the ejection [65]. Once the catalysis is started, the propulsion pushes the microjet with a constant force, that depends on the concentration of hydrogen peroxide in the medium the microjet is moving. Several speed control mechanisms for this type of microjets have been proposed in the literature. The first one used light to slow down the motion of the microjets [66]. Light, in fact, diminishes the local concentration of hydrogen peroxide and leads to a slower catalysis of fuel and, therefore, to less bubble formation. Another approach to speed control is based on thermoresponsive polymers. The opening and closing of the tube by slight temperature changes affect the accumulation of the oxygen bubbles [67]. When the temperature is increased, the microtube opens, and, as a result, the bubbles cannot accumulate in its cavity, stopping the motion of the microjet. On the other hand, when the temperature is decreased, the polymer film forms a microtube again, the bubbles starts to accumulate, and the forward motion starts.

In this work we do not enforce any direct control on the speed of the microjet. The electromagnetic system controls the orientation, whereas the forward motion is accomplished by the aforementioned thrust force generated by the ejecting oxygen bubbles.

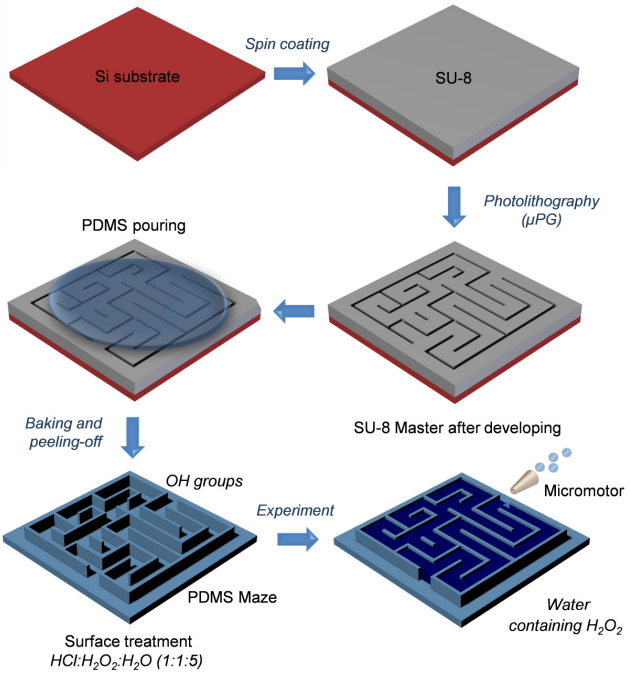

Fig. 7 Schematic of the maze fabrication steps and its surface treatment.

3.1.2 Maze fabrication and surface treatment

The mazes used in the first experiment consist of open microchannels in different configurations with thickness between 50 and 100 μm, and separation of 125, 250 and 500 μm. They were fabricated by rapid prototyping and PDMS technologies as described previously [68]. Briefly, a 50×50 mm^2 silicon substrate was spin coated for 30 s at 1000 and 2000 rpm with an acceleration of 300 rpm/s for obtaining 100 and 50 μm thicknesses, respectively, with a negative photoresist (SU8, Microchem, Germany) and patterned through a mask less technique (μPG-501, Heidelberg Instruments GmbH, Germany). First, the geometry was designed by using a digital CAD software, then the design was loaded in the device software and converted to μPG format. With a mask etch alignment procedure, the design was aligned to the substrate and was projected via micromirror array onto the photoresist by using a high power UV LED (emission wavelength of 390 nm), with an exposure time of 1500 ms. Then, the SU8 was baked according to the recommendations of MicroChem. The developing was made by immersion of the substrate in the respective developer (SU-8 Developer, Microchem, Germany) for 6 min with slight agitation. The reaction was then stopped with isopropanol, and finally dried with N_2 gun. After that, the silicon elastomer (Sylgrad 184, Dow Corning, Germany) was mixed with the curing agent at a ratio of 10:1 (w/w) and degassed by using a desiccator. Subsequently, the

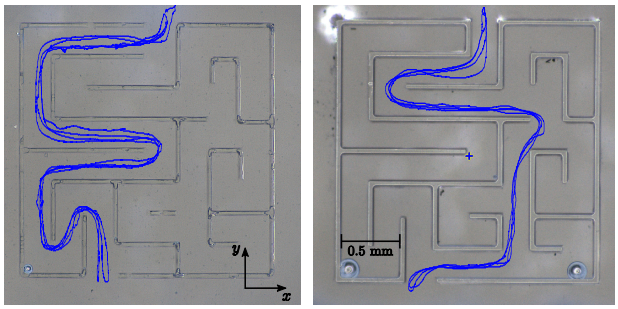

(a) (b)

Fig. 8 Trajectories for two representative runs of the microjet steering experiment in the two mazes considered. Each subject performed the task four times, steering the microjet through the maze from top to bottom and back two times.

PDMS was poured onto the SU8 master and baked for two hours at 65°C. Finally, the mazes were peeled-off from the master. To complete the fabrication and conditioning process, the mazes were immersed into an HCl:H_2O_2:H_2O (1:1:5) solution for 30 min, followed by a washing step in DI H_2O and dried with N_2 in order to create hydroxyl groups and confer hydrophilicity to the PDMS to avoid bubble forming at the moment of filling the microchannels with the micromotor containing solution. This process is summarized in Fig. 7.

3.2 Steering microjets in a structured remote environment

The first experiment aims at evaluating our teleoperation system in a structured remote environment composed of a 2.25×2.25 mm maze made of polydimethylsiloxane (PDMS), as detailed in Sec. 3.1.2.

3.2.1 Subjects

Sixteen subjects (15 males, 1 female, age range 20 - 32 years) took part in the experiment, all of whom were right-handed. Five of them had previous experience with haptic interfaces. None reported any deficiencies in their perception abilities. The experimenter explained the procedures and spent about two minutes adjusting the setup to be comfortable before the subject began the experiment. No practice trial was allowed.

3.2.2 Methods

The task consisted of steering a microjet through the maze, being as fast as possible, trying to avoid collisions with the maze walls, and taking the shortest path. According to the feedback condition considered, the subject was provided with kinesthetic and/or vibrotactile force feedback about the inertia of the controlled microjet and the collisions with the maze walls, as detailed below. The mazes employed are shown in Fig. 8. Eight subjects used the maze shown in Fig. 8a and eight the one shown in Fig. 8b. A video of the experiment is available as supplemental material. Three frames of the video are shown in Fig. 9.

Each subject made sixteen randomized repetitions of the microjet steering task, with four repetitions for each feedback condition proposed:

- kinesthetic-kinesthetic feedback, where kinesthetic force is used to render the inertia of the controlled microjet and the collisions between the reference point and the maze walls (condition KK);
- kinesthetic-vibrotactile feedback, where kinesthetic force is used to render the inertia of the controlled microjet and vibrotactile cues are used to render the collisions between the reference point and the maze walls (condition KV);
- visual substitution of force feedback, where information about the inertia of the microjet and about the collisions between the reference point and the maze walls is provided visually to the subject (condition S);
- no feedback about the inertia of the microjet and the collisions between the reference point and the maze walls (condition N).

In condition KK, the Omega haptic interface provides the subject with kinesthetic feedback about collisions of the reference point with the maze walls and about the inertia of the microjet. Kinesthetic force feedback $\mathbf{f_{c,k}}(\mathbf{t})$, responsible for rendering collisions of the reference point with the maze walls, is evaluated according to the popular god-object model [59], and the maze walls are modeled as spring-damper systems:

$$\mathbf{f_{c,k}}(\mathbf{t}) = -k_{c,k}(\mathbf{p_r}(\mathbf{t}) - \mathbf{p_{r,proxy}}(\mathbf{t})) - b_c\dot{\mathbf{p}}_\mathbf{r}(\mathbf{t}). \quad (6)$$

$k_{c,k} = 1000$ N/m is the elastic constant of the spring, $b_c = 5$ Ns/m is the damping coefficient, $\mathbf{p_r}(\mathbf{t}) \in \mathbb{R}^2$ is the current position of the reference point as controlled by the subject through the haptic interface, and $\mathbf{p_{r,proxy}}(\mathbf{t}) \in \mathbb{R}^2$ is the virtual location of the reference point, placed where the haptic interface point would be if the haptic interface and the walls were infinitely stiff (i.e., on the surface of the maze walls in our case) [59]. On the other hand, kinesthetic force feedback $\mathbf{f_{i,k}}(\mathbf{t})$, responsible for rendering the inertia of the microjet, is evaluated as if a spring-damper system connected the reference point and the microjet:

$$\mathbf{f_{i,k}}(\mathbf{t}) = -k_i(\mathbf{p_r}(\mathbf{t}) - \mathbf{p_j}(\mathbf{t})) - b_i\dot{\mathbf{p}}_\mathbf{r}(\mathbf{t}), \quad (7)$$

where $k_i = 100$ N/m is the elastic constant of the spring, $b_i = 5$ Ns/m is the damping coefficient, and $\mathbf{p_j}(\mathbf{t}) \in \mathbb{R}^2$ is the current position of the microjet as evaluated by the tracker. In this condition the subject feels an opposite force when trying to penetrate the maze walls and when moving the reference point far from the microjet (i.e., when the microjet is not fast enough to follow the reference point). Both forces are provided by the Omega 6 haptic interface.

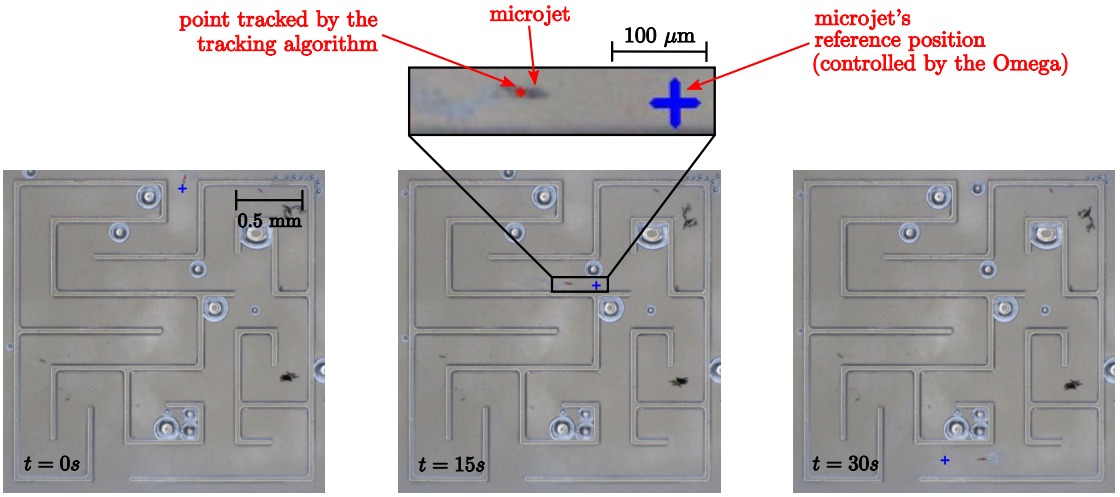

Fig. 9 Three frames from the video of the first experiment. The task consisted of steering the microjet through the maze being as fast as possible, trying to avoid collisions with the maze walls, and taking the shortest path. The blue cross indicates the microjet reference point that is linked to the position of the haptic interface end-effector. The red dot indicates the position of the microjet, as evaluated by the tracking algorithm. The full video is available as supplemental material.

In condition KV, the Omega haptic interface provides the subject with vibrotactile feedback about collisions of the reference point with the maze walls and kinesthetic feedback about the inertia of the microjet. Vibrotactile force feedback $\mathbf{f_{c,v}(t)}$, responsible for rendering collisions of the reference point with the maze walls, is again evaluated according to the god-object model [59], and the maze walls are modeled as spring systems:

$$\mathbf{f_{c,v}(t)} = k_{c,v}(\mathbf{p_r(t)} - \mathbf{p_{r,proxy}(t)}) \begin{bmatrix} \sin(2\pi f_h t) \\ \sin(2\pi f_v t) \end{bmatrix}. \quad (8)$$

$k_{c,v} = 200$ N/m is the elastic constant of the spring, and $f_h = 200$ Hz and $f_v = 150$ Hz are the frequencies of the vibrations when the collisions happen along the x and y directions, respectively (see Fig. 8). The amplitude of the vibration indicates the magnitude of the penetration inside the maze wall while its frequency indicates the direction of the collision. Frequency values are chosen to maximally stimulate the Pacinian corpuscle receptors [69], be easy to distinguish [70], and fit the master device specifications. The inertia is rendered as in condition KK (see eq. (7)). Both forces are again provided by the Omega 6 haptic interface.

In condition S, no force is fed back to the subject through the Omega haptic interface, and force feedback is substituted by a red line segment showing on the screen the vector $\mathbf{f_{c,k}(t)} + \mathbf{f_{i,k}(t)}$ as calculated in eqs. (6) and (7) (see Fig. 10). The pixel coordinates of the segment's endpoints are $(0,0)$ and $50(\mathbf{f_{c,k}(t)} + \mathbf{f_{i,k}(t)})$. This feedback technique, consisting of substituting force feedback with stimuli of another sensory modality (i.e., visual in this case), is known in haptics as sensory substitution. It is widely used in teleoperation to provide information about the forces exerted at the remote environment while guaranteeing the stability of the teleoperation loop (see Sec. 1).

Finally, in condition N, the system provides no information about the inertia of the microjet and the collisions between the reference point and the maze walls.

Visual feedback on the remote environment is always provided to the subjects (see Fig. 1), and the Omega 6 haptic interface is always used to provide the controller with the microjet's reference point. The passivity algorithm presented in [55] guarantees the stability of the control loop (see Sec. 2.3). The environment variables defined in eqs. (6), (7), and (8) have been selected by carrying out a pilot experiment enrolling three subjects (3 males, age range 25 - 29 years), who did not participate in the main experiment described in this section. They were asked to interact with the environment and modify at runtime the values of the considered variables (i.e., $k_{c,k}$, b_c, k_i, b_i, and $k_{c,v}$) until the haptic interaction felt as realistic as possible (e.g., touching the maze walls through the haptic interface felt like touching a real wall).

3.2.3 Results

We measure (1) task completion time, (2) percentage of time that the microjet is in contact with the maze walls, and (3) length of the microjet path. The task completion time is normalized by the average speed of the microjets considered in the experiment. A low value of these three metrics denotes the best performance. Similar metrics have been already used in the literature for different biomedical and microrobotic scenarios and applications. Diller et al. [71], for example, measured completion time and trajectory error of a path following task to evaluate the effectiveness of a magnetic system at independently control the motion of multiple microrobots in 3-D. The same metrics have been also used in [72]. Meli et al. [41] tested the effectiveness of kinesthetic and tactile

feedback in a robot-assisted surgical scenario and evaluated completion time, force exerted on the environment, and path length. Moody *et al.* [73] measured the performance of haptic feedback for a suturing task by evaluating completion time and force exerted on the environment. Finally, Pacchierotti et al. [74] evaluated completion time, force exerted on the environment, accuracy, and perceived effectiveness of tactile feedback in a palpation task using a da Vinci Surgical Robot (Intuitive Surgical Inc., USA).

Figure 11a shows the normalized average completion time for the four experimental conditions. All the data passed the Shapiro-Wilk normality test [75] and the Mauchly's Test of Sphericity [76]. A repeated-measure ANOVA [77] showed a statistically significant difference between the means of the four feedback conditions ($F(3,45) = 8.550$, $p < 0.001$, $a = 0.05$). Post hoc analysis with Bonferroni adjustments [78] revealed a statistically significant difference between conditions KK and N ($p = 0.003$), and KV and N ($p = 0.016$). Moreover, although the performance under condition S was not found significantly different from conditions KK and KV, comparison between them was very close to significance (KK vs. S with $p = 0.069$, KV vs. S with $p = 0.065$). The Bonferroni correction is used to reduce the chances of obtaining false-positive results when multiple pair-wise tests are performed on a single set of data.

Figure 11b shows the average percentage of time the microjet was in contact with the maze walls for the four experimental conditions. All the data passed the Shapiro-Wilk normality test and the Mauchly's Test of Sphericity. A repeated-measure ANOVA showed a statistically significant difference between the means of the four feedback conditions ($F(3,45) = 9.916$, $p < 0.001$, $a = 0.05$). Post hoc analysis with Bonferroni adjustments revealed a statistically significant difference between conditions KK and S ($p = 0.008$), KK and N ($p = 0.024$), KV and S ($p = 0.001$), and KV and N ($p = 0.020$).

Figure 11c shows the average length of the path the microjet took to exit the maze for the four experimental conditions. All the data passed the Shapiro-Wilk normality test and the Mauchly's Test of Sphericity. A repeated-measure ANOVA showed a statistically significant difference between the means of the four feedback conditions ($F(3,45) = 10.308$, $p < 0.001$, $a = 0.05$). Post hoc analysis with Bonferroni adjustments revealed a statistically significant difference between conditions KK and S ($p = 0.026$), KK and N ($p = 0.002$), KV and S ($p = 0.024$), and KV and N ($p = 0.009$).

In addition to the quantitative evaluation reported above, we also measured users' experience. Immediately after the experiment, subjects were asked to report the effectiveness of each feedback condition in completing the given task using bipolar Likert-type seven-point scales. Figure 11d shows the perceived effectiveness of the four feedback conditions. A Friedman test [79] showed a statistically significant difference between the means of the four feedback conditions ($\chi^2(3) = 42.702$, $p < 0.001$). The Friedman test is the non-parametric equivalent of the more popular repeated measures ANOVA. The latter is not appropriate here since the dependent variable was measured at the ordinal level. Post hoc analysis with Bonferroni adjustments revealed a statistically significant difference between conditions KK and S ($p = 0.030$), KK and N ($p = 0.045$), KV and S ($p < 0.001$), and KV and N ($p < 0.001$). Moreover, although condition KK was not found significantly different from condition KV, comparison between them was very close to significance ($p = 0.082$). Finally, subjects were asked to choose the condition they preferred the most. Condition KV was preferred by ten subjects, condition KK was preferred by four subjects, and condition N was preferred by two subjects. Subjects particularly appreciated the capability of condition KV to enable them to well discriminate between the force due to the inertia and the one due to the collision with the maze walls.

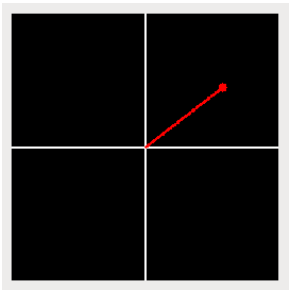

Fig. 10 In condition S, force feedback is substituted by visual feedback. A red line segment shows on the screen the force feedback $\mathbf{f_{c,k}}(\mathbf{t}) + \mathbf{f_{i,k}}(\mathbf{t})$ as calculated in eq. (6) and (7) for condition KK.

3.3 Steering microjets in an unstructured remote environment

In the experiment presented in Sec. 3.2, the remote environment is known and it is therefore easy to detect collisions with the maze walls. However, of course, this is not always the case, since in many scenarios we cannot retrieve such detailed a priori information about the environment the microjet is operating in. For this reason, we decided to carry out a second experiment aiming at evaluating the steering capabilities of our system in unstructured remote environments. The experimental setup is the same as described in Sec. 3.2 and shown in Fig. 1, but this time the remote environment is composed of randomly placed microstructures in the shapes of squares, equilateral triangles, and semicircles. The squares and triangles have sides of 0.15 mm and the semicircles have a diameter of 0.15 mm.

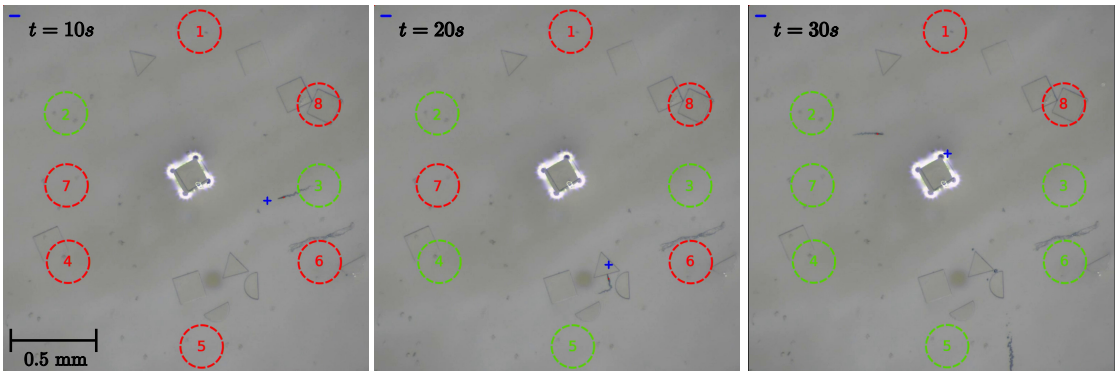

Fig. 12 Three frames from the video of the second experiment: The task consisted of exploring the remote environment by steering the microjet through a sequence of predefined locations, indicated in the screen as dashed circles. At the beginning, all the circles are red and they turn green as soon as the microjet enters them. As in the previous experiment, the blue cross indicates the microjet reference point, linked to the position of the haptic interface end-effector, while the red dot indicates the position of the microjet as evaluated by the tracking algorithm. The full video is available as supplemental material.

3.3.1 Subjects

Ten subjects (10 males, age range 22 - 30 years) took part in the experiment, all of whom were right-handed. Four of them had previous experience with haptic interfaces. None reported any deficiencies in their perception abilities. The experimenter explained the procedures and spent about two minutes adjusting the setup to be comfortable before the subject began the experiment. No practice trial was allowed.

3.3.2 Methods and Results

The task consisted of exploring the remote environment by steering a microjet through a sequence of predefined locations, indicated in the screen as dashed circles (see Fig. 12). At the beginning the circles were all red, and they turned green as the controlled microjet enters them. The task was considered completed when all the circles are green. The number and arrangement of the microstructures in the remote environment changed randomly between subjects (we had 12.7 $\pm$ 3.9 structures on average $\pm$ standard deviation). A video of the experiment is available as supplemental material.

Each subject completed the exploration task twice, once for each feedback condition proposed:

- Kinesthetic-kinesthetic feedback, where kinesthetic force is used to render both the inertia of the controlled microjet and the collisions between the microjet and the remote microstructures (condition KK).
- No feedback on the inertia of the microjet and on the collisions between the microjet and the remote microstructures (condition N).

In condition KK, the Omega haptic interface provides the subject with kinesthetic feedback about the collisions of the controlled microjet with the remote microstructures and about the inertia of the microjet. Conversely to the first experiment, this time we do not have any a priori information about the remote environment, so we propose to calculate the force feedback by evaluating the change in the speed of the controlled microjet during the task. For this reason, before the beginning of each task repetition, subjects were required to move the microjet in free space for 30 seconds, so to record its free-space speed v_{fs}. In this way, every time the controlled microjet enters in contact with one of the remote microstructures, its speed decreases, and we are therefore able to evaluate the kinesthetic force feedback $\mathbf{f_{c,k}(t)}$, responsible for rendering collisions of the microjet with the environment, as

$$\mathbf{f_{c,k}(t)} = -b_c(v_{fs} - v_j)\dot{\mathbf{p}}_\mathbf{r}(\mathbf{t}), \tag{9}$$

where $b_c = 6000$ N(s/m)^2, $\dot{\mathbf{p}}_\mathbf{r}(\mathbf{t})$ is the current velocity of the reference point as controlled by the subject, and $v_j = \|\dot{\mathbf{p}}_\mathbf{j}(\mathbf{t})\|$ is the current speed of the microjet. On the other hand, kinesthetic force feedback $\mathbf{f_{i,k}(t)}$, responsible for rendering the inertia of the microjet, is evaluated as if a spring-damper system was connected the reference point and the microjet:

$$\mathbf{f_{i,k}(t)} = -k_i(\mathbf{p_r(t)} - \mathbf{p_j(t)}) - b_i\dot{\mathbf{p}}_\mathbf{r}(\mathbf{t}), \tag{10}$$

where $k_i = 100$ N/m is the elastic constant of the spring, $b_i = 5$ Ns/m is the damping coefficient, and $\mathbf{p_j(t)} \in \mathbb{R}^2$ is the current position of the microjet as evaluated by the tracker. In this condition the user feels an increased viscosity every time the speed of the microjet is lower than the one registered in free space. Moreover, as in Sec. 3.2, the user feels an opposite force when moving the reference point far from the microjet (i.e., when the microjet is not fast enough to follow the reference point). Both forces are provided by the Omega 6 haptic interface.

In condition N, as in Sec. 3.2, the system provides no information about the inertia of the microjet and the collisions between the controlled microjet and the remote objects.

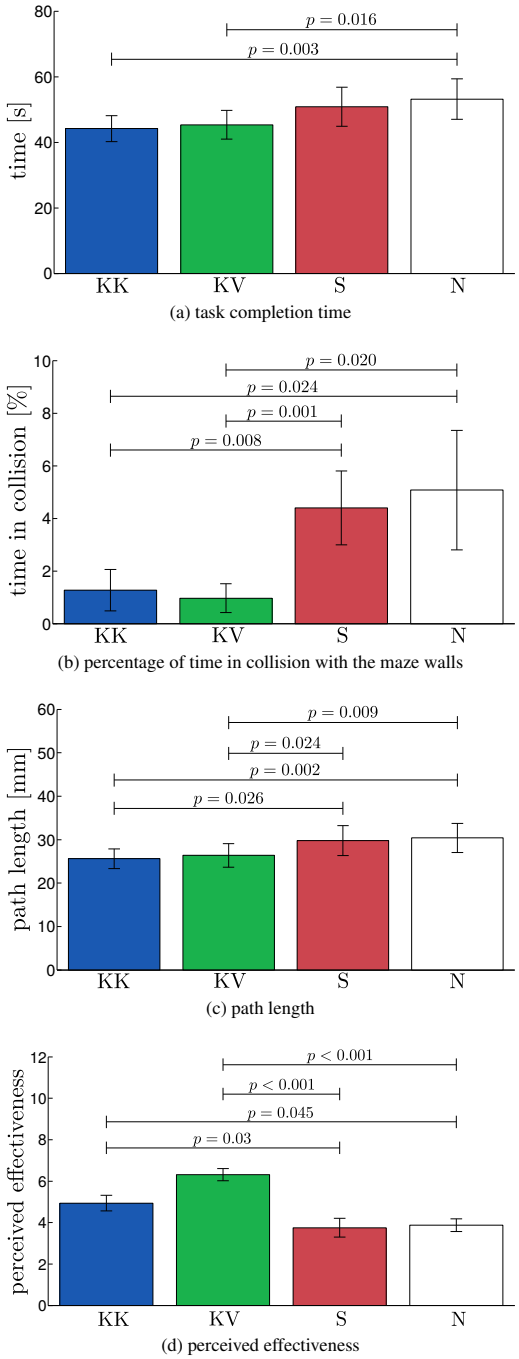

Fig. 11 Steering of microjets through a maze: Completion time, percentage of time that the microjet is in contact with the maze walls, length of the path, and perceived effectiveness are evaluated for the kinesthetic-only (KK), kinesthetic-vibrotactile (KV), sensory substitution (S), and no feedback (N) conditions (mean and 95% confidence interval are shown).

Visual feedback on the remote environment is again always provided to the subjects, and the Omega 6 haptic interface is always used to provide the controller with the microjet's reference point. The passivity algorithm presented in [55] guarantees again the stability of the control loop (see

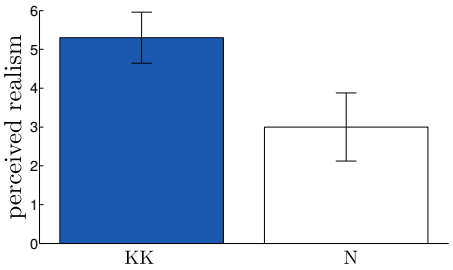

Fig. 13 Steering of microjets in an unstructured remote environment. Perceived realism of the interaction is evaluated for the kinesthetic (KK) and no feedback (N) conditions (mean and 95% confidence interval are shown).

Sec. 2.3). The environment variables defined in eqs. (9) and (10) have been selected by carrying out a pilot experiment analogous to the one described at the end of Sec. 3.2.2.

Immediately after the experiment, subjects were asked to report the perceived realism of each feedback condition in completing the given task using a bipolar Likert-type seven-point scale. Figure 13 shows the perceived realism of the two feedback conditions. A Wilcoxon Signed-Rank Test [80] revealed a statistically significant difference between the questions (Z = -2.469, $p = 0.014$). The Wilcoxon signed-rank test is the non-parametric equivalent of the more popular paired t-test. The latter is not appropriate here since the dependent variable is measured at the ordinal level.

4 Discussion

In order to test the effectiveness of our system, we carried out two types of experiments. The first one aimed at evaluating the steering capabilities of the proposed teleoperation system in a structured remote environment (see Sec. 3.2), while the second one aimed at evaluating the steering capabilities of our system in an unstructured remote environment (see Sec. 3.3). In both experiments, regardless of the feedback condition considered, all subjects were able to successfully complete the given task. Moreover, both experiments showed that providing haptic force feedback significantly improved the performance and the realism of the considered tasks. To the best of our knowledge, this is the first time that the effectiveness of haptics is shown for such a scenario.

In the first experiment, we proposed to provide the human operator with haptic force feedback, either kinesthetic or vibrotactile, about collisions of the reference point with the maze walls and the inertia of the microjet. Providing haptic feedback (conditions KK and KV) significantly improved the performance of the task with respect to not providing any kind of information about the forces exerted (condition N) in all the considered metrics. It also significantly outperformed sensory substitution of force feedback (condition S) in all the metrics but completion time. No statistical difference was shown between the two conditions providing haptic feedback

(KK and KV). However, condition KV was preferred by ten subjects out of eighteen, and subjects particularly appreciated the capability of condition KV to enable them to well discriminate between the force due to the inertia and the one due to the collision with the maze walls. This enhanced discrimination capability of condition KV has been already demonstrated in the literature for needle insertion, but never for applications at the micro level. Pacchierotti et al. [28], for example, proposed a haptic system to steer flexible needles in soft tissue. The master haptic interface provides the operator with mixed kinesthetic-vibrotactile navigation cues to guide the needle toward the target. The mixed kinesthetic-vibrotactile condition outperformed both sensory substitution via visual feedback and kinesthetic feedback only. Ramos et al. [58] combined vibrotactile and kinesthetic force feedback to render, at the same time, forces generated by the collision of the slave tool with the remote environment and forces generated by the action of active constraints [81]. The condition mixing vibrotactile and kinesthetic feedback outperformed the one providing kinesthetic feedback only and was preferred by most subjects. Finally, it is also worth noticing that in the first experiment we provided force feedback about collisions of the reference point with the maze walls, while it may seem more natural to provide force feedback about collisions of the microjet with the maze walls. However, the position of the microjet as estimated by the tracking algorithm is subject to unanticipated changes and this, together with the high stiffness value $k_{c,k}$ assigned to the maze walls (see eq. (6)), may lead to undesirable abrupt changes in the position of the haptic device end-effector. For this reason, in this first experiment we considered the collisions of the reference point. However, in the second experiment, where the rendering policy is different, we take into account the collisions of the microjet with the remote environment.

In the second experiment, we propose to provide the human operator with kinesthetic force feedback about the inertia of the controlled microjet and the collisions between the microjet and the remote environment, which was randomly filled with microstructures. Providing haptic feedback (condition KK) significantly improved the perceived realism of the task with respect to not providing any kind of information about the forces exerted (condition N). The force feedback considered for this experiment is based on the change of speed of the microjet and this is the first time that such a rendering policy is used in applications at the micro level. This policy could have been, of course, also used in the experiment with the maze, where the remote environment was known. However, the a priori knowledge of the remote environment enabled us to provide a more effective and compelling force feedback. On the other hand, we often do not have such information, and therefore the speed-based approach employed in the second experiment is still a valuable technique. Since in this experiment the force feedback is evaluated according to the change in speed of the microjet, the tracking algorithm plays here a paramount role. Without a reliable and robust technique to track the position of the microjet, in fact, it would have not been possible to achieve such a result. The tracking task is particularly challenging is our situation, where we need to deal with inconsistent shapes such as our microjets surrounded by oxygen bubble trails. The fact that all the subjects were able to successfully complete the task with high perceived realism is therefore also an indicator of the quality and robustness of the enforced tracking technique.

Results proved our system to be an effective and intuitive solution for steering self-propelled micromotors in various environments. Twenty-six subjects, with no prior experience, managed to easily complete the considered tasks and found our system easy to learn and easy to use. Moreover, haptic feedback was proven to be an effective tool to significantly improve the performance and realism of such a system.

5 Conclusion and future work

In this work we presented a novel teleoperation system with haptic force feedback for the steering of self-propelled micromotors, which we refer to as microjets. The human operator is able to intuitively steer the microjets using the end-effector of a grounded haptic interface, while being provided, through the same end-effector, with haptic feedback about the forces exerted at the remote environment. The system is shown in Fig. 1. We carried out two experiments, enrolling twenty-six subjects. The first experiment aimed at evaluating the steering capabilities of the proposed teleoperation system in a structured remote environment composed of a 2.25×2.25 mm maze, while the second experiment aimed at evaluating the steering capabilities of our system in an unstructured remote environment composed of randomly placed microstructures. In both experiments, regardless of the feedback condition considered, all subjects were able to successfully complete the given task. However, both experiments showed that providing haptic force feedback significantly improved the performance and the realism of the considered tasks. Moreover, conditions employing haptic feedback were also significantly preferred by the users.

In the near future, we will focus on investigating the practical translational aspects of the proposed teleoperation system for biomedical applications. In the current form, in fact, our catalytic microjets are not suitable for biomedical applications, since their fuel, hydrogen peroxide, is not biocompatible. In this respect, Gao et al. [82] very recently reported an *in vivo* study of zinc-based artificial micromotors in a living organism using a mouse model. They demonstrated that the acid-driven propulsion in the mouse stomach effectively enhances the binding and retention of the motors as well as of cargo payloads on the stomach wall. Moreover, the body of the micromotors gradually dissolved in the

gastric acid, releasing the carried payload and leaving no toxic residue behind. In addition to exploring the usage of biocompatible fuels, we are also planning to substitute the high-resolution camera with an ultrasound imaging system, so to be able to track the position of the controlled microjet and other self-propelled microsized agents in biological fluid. In this respect, Sanchez et al. [25] already presented an algorithm for the closed-loop control of self-propelled microjets using feedback extracted from B-mode ultrasound images, and Khalil et al. [26] demonstrated the effectiveness of our magnetic control system in steering self-propelled microjets against fluidic flows. With a flow rate of 2.5 μl/min applied against the direction of the microjets, the control system positioned the microjets at an average velocity of 90 μm/s and within an average region of convergence of 600 μm.

Finally, we would like to be able to control the position and speed of the microjets in 3-dimensional space, extending the experimental evaluation to multi-level mazes. We are also interested in testing different types of haptic stimuli (e.g., skin-stretch, pin-arrays) and sensory substitution techniques (e.g., visual, audio), with the objective of improving the results registered in this work. Future applications of the system include targeted drug delivery of microsized agents and nanocapsules, as well as micromanipulation of artificial objects. It has been in fact shown that self-propelled microjets can selectively transport relatively large amounts of particles on-a-chip and Murine Cath.a-differentiated cells [4].

Acknowledgements The authors thank Alonso Sanchez for his help in setting up the tracking and control systems, and Frank van den Brink and Momen Abayazid for their help in making the video.

References

1. A.A. Solovev, Y. Mei, E.B. Urena, G. Huang, O.G. Schmidt, Small **5**(14), 1688 (2009)
2. I.S.M. Khalil, V. Magdanz, S. Sanchez, O.G. Schmidt, M. S, Applied Physics Letters **103**(17), 172404 (2013)
3. S.P. Woods, T.G. Constandinou, in *Proc. International Conference of the IEEE Engineering in Medicine and Biology Society* (2011), pp. 7372–7375
4. S. Sanchez, A.A. Solovev, S. Schulze, O.G. Schmidt, Chemical Communications **47**(2), 698 (2011)
5. A.A. Solovev, S. Sanchez, M. Pumera, Y.F. Mei, O.G. Schmidt, Advanced Functional Materials **20**(15), 2430 (2010)
6. L. Zhang, T. Petit, K.E. Peyer, B.J. Nelson, Nanomedicine: Nanotechnology, Biology and Medicine **8**(7), 1074 (2012)
7. S. Balasubramanian, D. Kagan, C.M. Jack Hu, S. Campuzano, M.J. Lobo-Castañon, N. Lim, D.Y. Kang, M. Zimmerman, L. Zhang, J. Wang, Angewandte Chemie International Edition **50**(18), 4161 (2011)
8. D. Kagan, S. Campuzano, S. Balasubramanian, F. Kuralay, G.U. Flechsig, J. Wang, Nano letters **11**(5), 2083 (2011)
9. L. Soler, V. Magdanz, V.M. Fomin, S.O. Sanchez, O.G. Schmidt, ACS Nano **7**, 9611 (2013)
10. W. Xi, A.A. Solovev, A.N. Ananth, D.H. Gracias, S. Sanchez, O.G. Schmidt, Nanoscale **5**, 1294 (2013)
11. M. Matteucci, M. Casella, M. Bedoni, E. Donetti, M. Fanetti, F. De Angelis, F. Gramatica, E. Di Fabrizio, Microelectronic Engineering **85**(5), 1066 (2008)
12. A.A. Solovev, W. Xi, D.H. Gracias, S.M. Harazim, S.M. Deneke, S. Sanchez, O.G. Schmidt, ACS Nano **6**, 1751 (2012)
13. M. Guix, J. Orozco, M. Garcia, W. Gao, S. Sattayasamitsathit, A. Merkoci, A. Escarpa, J. Wang, ACS Nano **6**, 4445 (2012)
14. F. Kuralay, S. Sattayasamitsathit, W. Gao, A. Uygun, A. Katzenberg, J. Wang, Journal of the American Chemical Society **134**, 15217 (2012)
15. J. Orozco, A. Corts, G. Cheng, S. Sattayasamitsathit, W. Gao, X. Feng, Y. Shen, J. Wang, Journal of the American Chemical Society **135**, 5336 (2013)
16. Z. Wu, Y. Wu, W. He, X. Lin, J. Sun, Q. He, Angewandte Chemie International Edition **52**, 7000 (2013)
17. B.J. Nelson, I.K. Kaliakatsos, J.J. Abbott, Annual review of biomedical engineering **12**, 55 (2010)
18. S. Fournier-Bidoz, A.C. Arsenault, I. Manners, G.A. Ozin, Chemical Communication **4**, 441 (2005)
19. I.K. B. Nelson, J. Abbott, Annual Review of Biomedical Engineering **12**, 55 (2010)
20. W.F. Paxton, S. Sundararajan, T.E. Mallouk, A. Sen, Angewandte Chemie International Edition **45**(33), 5420 (2006)
21. R. Golestanian, T.B. Liverpool, A. Ajdari, Physical review letters **94**(22), 220801 (2005)
22. J.M. Catchmark, S. Subramanian, A. Sen, Small **1**(2), 202 (2005)
23. S. Sanchez, A.N. Ananth, V.M. Fomin, M. Viehrig, O.G. Schmidt, Journal of the American Chemical Society **133**(38), 14860 (2011)
24. I.S.M. Khalil, V. Magdanz, S. Sanchez, O.G. Schmidt, S. Misra, PLoS One **9**(2), e83053 (2014)
25. A. Sanchez, V. Magdanz, O.G. Schmidt, S. Misra, in *Proc. 5th IEEE RAS & EMBS International Conference on Biomedical Robotics and Biomechatronics* (2014), pp. 169–174
26. I.S.M. Khalil, V. Magdanz, S. Sanchez, O.G. Schmidt, S. Misra, IEEE Transactions on Robotics **30**(1), 49 (2014)
27. J. Troccaz, Y. Delnondedieu, Mechatronics **6**(4), 399 (1996)
28. C. Pacchierotti, M. Abayazid, S. Misra, D. Prattichizzo, IEEE Transactions on Haptics **7**(4), 551 (2014)
29. M. Jakopec, F.R. y Baena, S.J. Harris, P. Gomes, J. Cobb, B.L. Davies, IEEE Trans. Robot. Autom **19**(5), 902 (2003)
30. K. Hashtrudi-Zaad, S.E. Salcudean, Robotics and Automation, IEEE Transactions on **18**(1), 108 (2002)
31. A.M. Okamura, Industrial Robot: An International Journal **31**(6), 499 (2004)
32. A.M. Okamura, Current opinion in urology **19**(1) (2009)
33. E.P. Westebring-Van Der Putten, R.H.M. Goossens, J.J. Jakimowicz, J. Dankelman, Minimally Invasive Therapy & Allied Technologies **17**(1), 3 (2008)
34. O.A.J. van der Meijden, M.P. Schijven, Surg. Endosc. **23**(6), 1180 (2009)
35. A. Wedmid, E. Llukani, D.I. Lee, BJU Int. **108**, 1028 (2011)
36. D. Prattichizzo, C. Pacchierotti, S. Cenci, K. Minamizawa, G. Rosati, in *Haptics: Generating and Perceiving Tangible Sensations* (2010), pp. 125–130
37. D. Prattichizzo, C. Pacchierotti, G. Rosati, IEEE Transactions on Haptics **5**(4), 289 (2012)
38. M.J. Massimino, T.B. Sheridan, Human Factors: The Journal of the Human Factors and Ergonomics Society **36**(1), 145 (1994)
39. C. Pacchierotti, F. Chinello, M. Malvezzi, L. Meli, D. Prattichizzo, in *Haptics: Perception, Devices, Mobility, and Communication* (2012), pp. 373–382
40. C.R. Wagner, R.D. Howe, N. Stylopoulos, in *Proc. International Symposium on Haptic Interfaces for Virtual Environment and Teleoperator Systems* (2002), pp. 354–355
41. L. Meli, C. Pacchierotti, D. Prattichizzo, IEEE Trans. Biomed. Eng **61**(4), 1318 (2014)

42. S.E. Salcudean, S. Ku, G. Bell, in *Proc. First Joint Conference on Computer Vision, Virtual Reality and Robotics in Medicine and Medial Robotics and Computer-Assisted Surgery* (1997), pp. 789–798
43. A. Kazi, Presence: Teleoperators & Virtual Environments **10**(5), 495 (2001)
44. L. Moody, C. Baber, T.N. Arvanitis, et al., Studies in health technology and informatics **85**, 304 (2002)
45. C.W. Kennedy, T. Hu, J.P. Desai, A.S. Wechsler, J.Y. Kresh, Cardiovascular Engineering **2**(1), 15 (2002)
46. A. Pillarisetti, M. Pekarev, A.D. Brooks, J.P. Desai, IEEE Transactions on Automation Science and Engineering **4**(3), 322 (2007)
47. N. Ando, P. Korondi, H. Hashimoto, IEEE/ASME Transactions on Mechatronics **6**(4), 417 (2001)
48. M. Mehrtash, N. Tsuda, M.B. Khamesee, IEEE/ASME Transactions on Mechatronics **16**(3), 459 (2011)
49. A. Bolopion, S. Régnier, IEEE Transactions on Automation Science and Engineering **10**(3), 496 (2013)
50. A. Ghanbari, B. Horan, S. Nahavandi, X. Chen, W. Wang, IEEE Systems Journal **8**(2), 371 (2014)
51. A. van der Schaft, *L2-gain and passivity techniques in nonlinear control* (Springer Verlag, 2000)
52. G. Niemeyer, J.J.E. Slotine, The International Journal of Robotics Research **23**(9), 873 (2004)
53. J. Ryu, D. Kwon, B. Hannaford, IEEE Transactions on Robotics and Automation **20**(2), 365 (2004)
54. J. Kim, J. Ryu, The International Journal of Robotics Research **29**(6), 666 (2010)
55. M. Franken, S. Stramigioli, S. Misra, C. Secchi, A. Macchelli, IEEE Trans. Robot. **27**(4), 741 (2011)
56. R.E. Schoonmaker, C.G. Cao, in *Proc. IEEE International Conference on Systems, Man and Cybernetics*, vol. 3 (2006), vol. 3, pp. 2464–2469
57. M. Kitagawa, D. Dokko, A.M. Okamura, D.D. Yuh, The Journal of thoracic and cardiovascular surgery **129**(1), 151 (2005)
58. A. Ramos, C. Pacchierotti, D. Prattichizzo, in *Proc. IEEE World Haptics Conference (WHC)* (2013), pp. 473–478
59. C.B. Zilles, J.K. Salisbury, in *Proc. IEEE/RSJ International Conference of Intelligent Robots and Systems* (1995)
60. R.M. Haralock, L.G. Shapiro, *Computer and robot vision, Addison-Wesley Longman Publishing Co., Inc.* (1991)
61. M.S. Arulampalam, S. Maskell, N. Gordon, T. Clapp, IEEE Transactions on Signal Processing **50**(2), 174 (2002)
62. S. Baker, I. Matthews, International journal of computer vision **56**(3), 221 (2004)
63. V.I. Utkin, H. Chang, Mathematical problems in Engineering **8**, 4 (2002)
64. A.S. Bahaj, P.A.B. James, F.D. Moeschler, IEEE Transactions on Magnetics **32**, 5133 (1996)
65. V.M. Fomin, M. Hippler, V. Magdanz, L. Soler, S. Sanchez, O.G. Schmidt, IEEE Transactions on Robotics **30**(1), 40 (2014)
66. A.A. Solovev, E.J. Smith, C.C. Bof'Bufon, S. Sanchez, O.G. Schmidt, Angewandte Chemie International Edition **50**(46), 10875 (2011)
67. V. Magdanz, G. Stoychev, L. Ionov, S. Sanchez, O. Schmidt, et al., Angewandte Chemie International Edition **53**(10), 2673 (2014)
68. Y. Xia, G.M. Whitesides, Annual review of materials science **28**(1), 153 (1998)
69. R.W. Cholewiak, A.A. Collins, in *The Psychology of Touch, Laurence Erlbaum Associates* (1991), pp. 13–60
70. K.A. Kaczmarek, J.G. Webster, P.B. y. Rita, W.J. Tompkins, IEEE Transactions on Biomedical Engineering **38**(1), 1 (1991)
71. E. Diller, J. Giltinan, M. Sitti, The International Journal of Robotics Research **32**(5), 614 (2013)
72. E. Diller, S. Floyd, C. Pawashe, M. Sitti, IEEE Transactions on Robotics **28**(1), 172 (2012)
73. L. Moody, C. Baber, T.N. Arvanitis, et al., Studies in health technology and informatics pp. 304–310 (2002)
74. C. Pacchierotti, D. Prattichizzo, K.J. Kuchenbecker, IEEE Transactions on Biomedical Engineering. In Press (2015)
75. S.S. Shapiro, M.B. Wilk, Biometrika pp. 591–611 (1965)
76. J.W. Mauchly, The Annals of Mathematical Statistics **11**(2), 204 (1940)
77. R. Gueorguieva, J.H. Krystal, Archives of general psychiatry **61**(3), 310 (2004)
78. O.J. Dunn, Journal of the American Statistical Association **56**(293), 52 (1961)
79. M. Friedman, Journal of the American Statistical Association **32**(200), 675 (1937)
80. F. Wilcoxon, Biometrics bulletin pp. 80–83 (1945)
81. J.J. Abbot, P. Marayong, A.M. Okamura, Robotics research **28**(1), 49 (2007)
82. W. Gao, R. Dong, S. Thamphiwatana, J. Li, W. Gao, L. Zhang, J. Wang, ACS Nano **9**(1), 117 (2015). DOI 10.1021/nn507097k